The International Journal of Advanced Manufacturing Technology (2022) 122:4375–4387
https://doi.org/10.1007/s00170-022-09884-9

ORIGINAL ARTICLE

# Numerical and experimental study on protective film removal towards the automation of flexible electronics assembly

**Vito Basile[1] · Gianmauro Fontana[2] · Francesco Modica[1] · Marcello Valori[1] · Lara Rebaioli[2] · Serena Ruggeri[2] · Simone Pio Negri[1] · Irene Fassi[2]**

Received: 14 July 2022 / Accepted: 28 July 2022 / Published online: 12 September 2022


**Abstract**
Flexible electronics is one of the most promising trends in the electronics industry, with increasing implementations in several application fields. However, in industrial applications, the assembly of film-based coverlays is still performed manually, representing a bottleneck in the whole production cycle, a source of defects caused by human errors, and introducing fatiguing tasks, such as the removal of the protective film covering the base material. In a novel methodology, this latter challenge is achieved by relying on the mechanical action of a rotating tool impacting the protective film. Such a process is typically stochastic and dependent on several parameters related to the tool-coverlay interaction, and the flexibility of film-type introduces further complexity. The aim of this paper is to investigate the influence of working conditions on the reliability of the process (i.e., success rate of the removal of the protective film). Finite element method (FEM) simulations are used to investigate and assess the stiffness exhibited by the component in response to the impacting force; therefore, a favorable gripping configuration is identified. An experimental campaign of the automated process is presented, aimed at assessing the effects of process parameters (tool rotating speed, adhesive thickness, approaching speed) on the protective film detachment. The results show that the process is predominantly affected by component-specific parameters, which, in turn, are significantly dependent on material supply conditions. Finally, useful insights are drawn to optimize the process and improve the design of the gripper of the robotized workcell.

**Keywords** Flexible film · Peeling · Flexible electronics · Coverlay assembly · Protective film removal · Mechanical film simulation

## 1 Introduction

In the last decades, the electronic sector underwent a huge technological growth, enabled by advancements in material science, applied physics, manufacturing technologies, etc. In addition, market demands are continually pushing forward towards some disruptive paradigms: (i) miniaturization and ultra-large scale integration; (ii) embedded component technology (ECT); (iii) molded interconnect devices (MIDs) and 3D electronics; (iv) flexible and

✉ Gianmauro Fontana
gianmauro.fontana@stiima.cnr.it

Vito Basile
vito.basile@stiima.cnr.it

Francesco Modica
francesco.modica@stiima.cnr.it

Marcello Valori
marcello.valori@stiima.cnr.it

Lara Rebaioli
lara.rebaioli@stiima.cnr.it

Serena Ruggeri
serena.ruggeri@stiima.cnr.it

Simone Pio Negri
simone.negri@stiima.cnr.it

Irene Fassi
irene.fassi@stiima.cnr.it

[1] CNR-STIIMA National Research Council - Institute of Intelligent Industrial Technologies and Systems for Advanced Manufacturing, 70124 Bari, Italy

[2] CNR-STIIMA National Research Council - Institute of Intelligent Industrial Technologies and Systems for Advanced Manufacturing, 20133 Milano, Italy

deformable electronics; and (v) low environment impact and circular economy, still chasing higher and higher levels of performance and reliability [1–4].

Flexible and rigid-flexible electronics find extensive applications in various fields such as biomedical, consumer electronics, sensors, automation, aerospace, and automotive. Some products that are advantaged from flexible electronics (FE) are sensors for health monitoring, implantable devices, miniaturized tools and instruments, wearable devices, smartwatches, and TVs [5]. Indeed, this technological niche dominates the field of durable, foldable, thin and lightweight products [5]. Other advantages of FE compared with traditional rigid printed circuit boards (PCBs) are complex 3D shaping and wiring, footprint reduction, and volume optimization. In FE, conductors lay on a thin flexible dielectric support, typically made of polyimide (PI), while insulation and protection are guaranteed by another PI film superimposed on the substrate. In rigid-flexible PCBs, portions of rigid circuits are connected by means of thin flexible circuits allowing folding of the different rigid portions along the connection axis.

The flexible portion is protected and electrically insulated by an additional thin flexible component called "coverlay," assembled between the rigid portions of the flexible printed circuit board (FPCB). Leveraging their mechanical properties, mainly strength and durability, film coverlays are preferred among the different available types (film, screen printable, photoimageable), mainly due to the reliability of the final products [6].

Due to the disruptive spread of electronic devices, the full automation of the manufacturing processes is a fundamental target to be pursued. The production of traditional electronics, i.e., rigid PCB, is characterized by high throughput, achieved via high-performance automation and optimized processes and materials; on the other hand, latest electronic products pose new manufacturing automation challenges. Accordingly, the digitalization of printing processes in conjunction with the assembly of discrete components has been the object of research interest in the last years [7, 8]. In particular, regarding flexible electronics, it is worth mentioning the increasing use of the most recent laser-based techniques [9]. The production of FPCB is still based on the assembly of flexible PI layers as substrates and protections of copper-based circuits. In the automated process, some critical issues are still unsolved, related in particular to those phases in which flexible components are manipulated and assembled with high accuracy. In particular, the assembly of film coverlays is still often performed manually, requiring a significant cognitive load from the operators due to the required level of accuracy and repeatability.

### 1.1 Coverlay assembly process

This section briefly introduces the film coverlay assembly steps. The base material is the same of the flexible substrate (Kapton polyimide), with thickness spanning from 25 to 127 μm; the components typically have complex contours and surface extension in the order of several $cm^2$, in compliance with the specific design requirements. The raw material presents one side coated by a 25–75-μm-thick acrylic adhesive, covered by a 50-μm-thick polyethylene (PE) protective film.

The production output of the base material is usually in the form of coils, from which sheets are obtained and supplied for FPCB production. The coverlays with design-specific contours are preliminarily laser trimmed from these sheets, according to the PCB design [10]. The bonding on the flexible layer is performed in four phases: (1) protective film removal; (2) accurate positioning of the coverlay on the substrate; (3) fixation, by heating small portions (2 or 3 points or small areas) of the coverlay to avoid further displacements after the release; and (4) adhesive activation by thermo-mechanical curing of the acrylic adhesive resin. The final lamination of the whole board is performed into a press where all the rigid and flexible layers are accurately assembled to form the build-up (or stack-up) [11]. The coverlay assembly process is schematically depicted in Fig. 1, while a real case of FPCB and coverlay assembly on the flexible layer is presented in Fig. 2.

Among the phases for the coverlay application (Fig. 1), the first one—protective film removal—is the most critical [1, 12, 13] from the perspective of process automation for several reasons: (i) the intrinsic high flexibility of films; (ii) complexity of the interaction among gripper and coverlay; and (iii) complex geometry and small thickness of films. This task consists in the detachment of a film from another with an adhesive layer interposed in between. It is worth observing that only mechanical removal methods are eligible (i.e., by applying a suitable force), since other methods (chemical, thermal) can damage either the adhesive or the Kapton PI coverlay.

In roll-to-roll fabrication approaches, the removal of a bonded protective film relies on exploiting the action of needles [14] or insertion tools working as blades [15], in combination with high bending angles of the continuous film. When the material either is not a film or is not handled with a roll-to-roll approach, the removal of a protective film becomes tricky, as it usually needs a trial-and-error approach, in particular, to trigger the

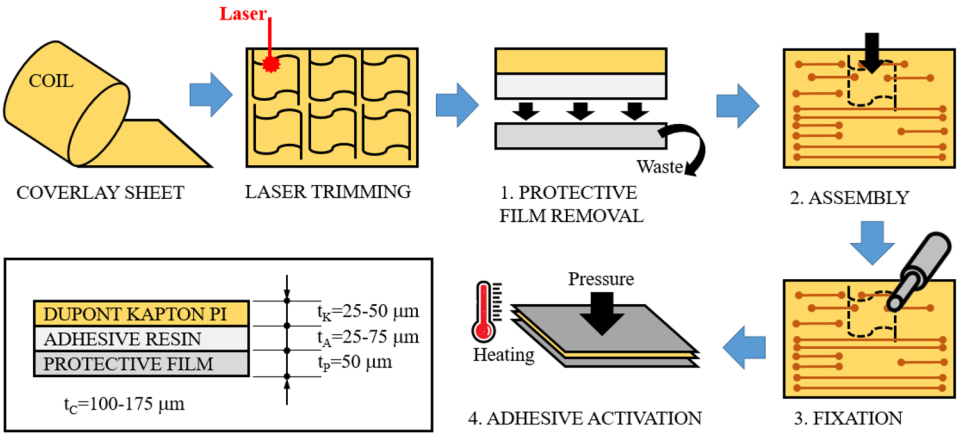


**Fig. 1** Coverlay assembly process

detachment, which is the most challenging task. Recent literature addressed other similar issues belonging to different application fields. A pilot case is represented by the removal of backing foils of papers from the prepreg raw material used for the processing of sheet molding compound: in [16], triggering the separation by injecting air and exploiting mechanical bending is investigated; in [17], the use of brushes, rubber friction, adhesive tapes. or hot malts is also evaluated; in [18], a gripper is proposed, combining vacuum and mechanical actions to achieve the removal. The issue of removing coverlay protective film presents the further complication of the high flexibility of the parental material. The methodology under investigation for the automation of coverlay removal process relies on the mechanical action of a rotating tool as a generator of the triggering force (see Fig. 3), identified as "pre-peeling" phase, followed by "peeling" completion by means of a vacuum cup [12, 13]. Despite promising as enabling the immediate detachment of the edge of the protective film, the process turns to be stochastic and extremely variable in terms of protective film-detached portion. To overcome these issues and reduce the uncertainty, numerical analysis, based on finite element method (FEM), can be exploited to highlight criticalities on FPCB, suggesting solutions and allowing a higher process comprehension [19, 20].

## 1.2 Paper contribution

The aim of the current work is to investigate the influence of process parameters and the most relevant mechanical factors affecting the reliability of the pre-peeling process, considering its full automation. The approach is based on both numerical and experimental investigations, as schematized in Fig. 4. The former are used to assess the stiffness exhibited by the coverlay in response to the triggering force in different gripping configurations. Therefore, the optimal gripping configuration is obtained, mainly characterized by the coverlay portion overhanging out of the gripper envelope to enable the pre-peeling; preliminary tests are performed to verify the numerical result. The test campaign aims to analyze the main parameters' influence on the pre-peeling success (component configuration and parameters characterizing the material and the process). The twofold approach enables the assessment of the impact of some parameters allowing the extraction of relevant key-drivers to improve the setup and the task execution.

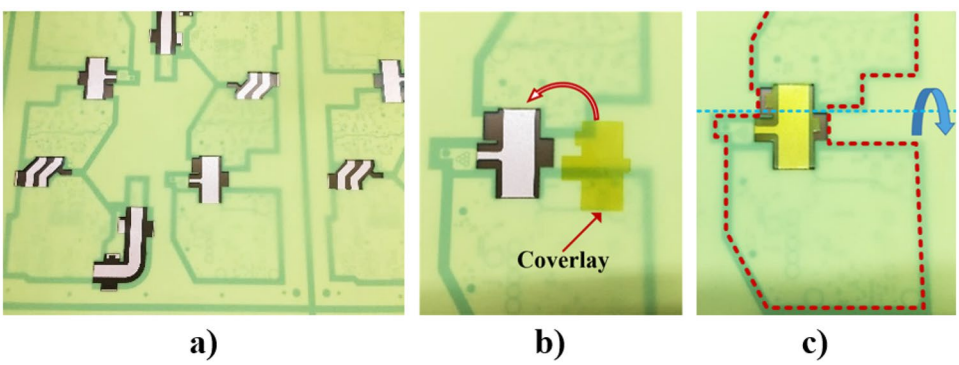


**Fig. 2** Coverlay application on an FPCB. **a** Flexible layer without coverlay. **b** Positioning of the coverlay. **c** Flexible layer with coverlay. In (**c**), the red dashed lines identify the contours of the two rigid portions connected by the flexible layer. (Courtesy of Somacis S.p.A., Italy)

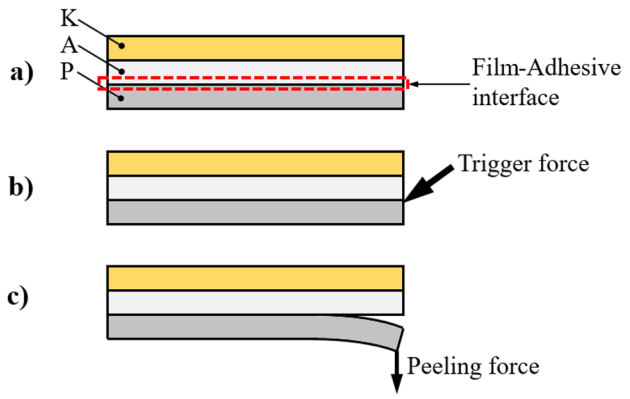


**Fig. 3** Schematic steps for coverlay removal

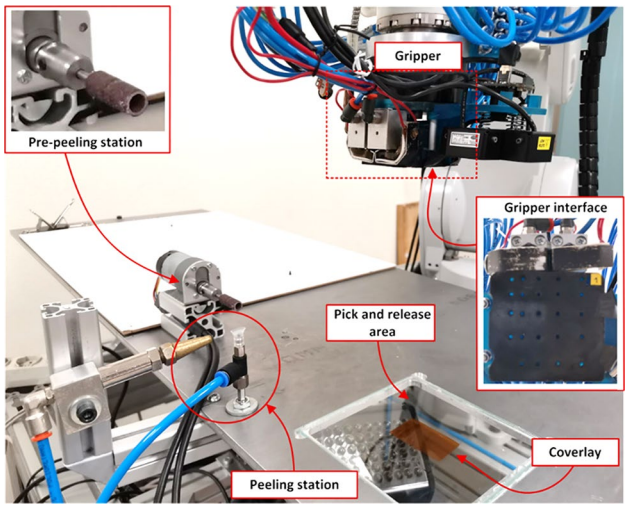


**Fig. 5** The workcell developed for automating the coverlay application process. Detail views: (top left) The pre-peeling station with the rotating sanding drum; (top right) The custom gripper and the gripper interface, with the pattern of vacuum orifices

The paper is organized as follows. Section 2 reports the numerical simulations, the automation solution for mechanical peeling of the coverlay, the related experimental setup and procedure, and the design of experiments (DOE). In Sect. 3, the experimental results are presented and discussed, supported by further FEM simulations. Finally, conclusions are reported in Sect. 4.

## 2 Materials and methods

The strategy for the protective film removal consists in two sub-phases, identified respectively as "pre-peeling" and "peeling." Firstly, the detachment of the protective film is obtained by the action of a rotating sanding drum impacting with coverlay edge. To accomplish this, the coverlay pick is configured so that a portion of the coverlay overhangs out of the gripper (cantilever configuration); the robot task is programmed in order to move the coverlay edge towards the sanding drum, enabling the impact and the consequent detachment. A first study about the interaction of coverlay and sanding drum was proposed in [12], and a further investigation of other process parameters was reported in [13]. The "peeling" is then obtained by the combined action of a suction cup and an air stream. Both the numerical analyses and the experimental campaign presented in this paper are focused on the "pre-peeling" phase, representing the most challenging step of the process.

In Fig. 5, the robotized workcell realized on purpose is shown, with the "pre-peeling" and "peeling" stations highlighted. It exploits a multi-hole vacuum gripper, mounted on the 6-DOFs robot arm Mitsubishi RV-4FL to manipulate the coverlay; a 6-axis force sensor interfaces the robot with the gripper, ensuring the parallelism between the bottom surface of the gripper and the surface where the coverlay is placed. The pick and release area consists of a transparent glass substrate with a vision system, measuring from the bottom the coverlay pose (to support the picking phase) and the portion of its area detached after the pre-peeling. The pre-peeling station consists of a sanding

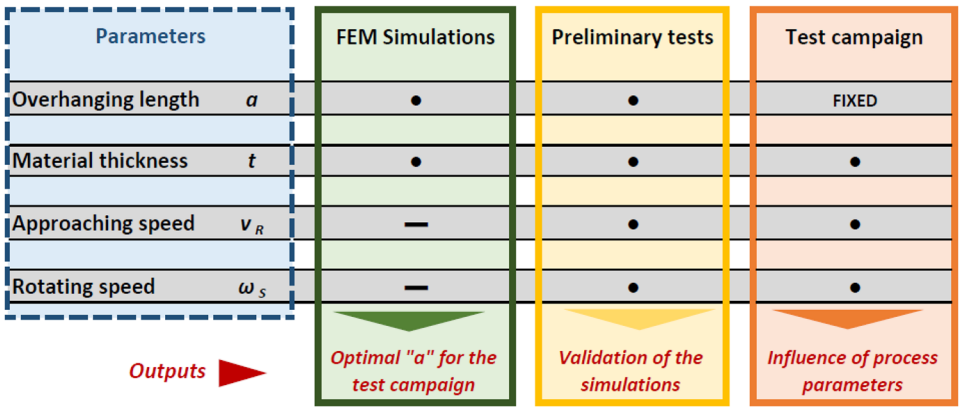


**Fig. 4** Schematic of the investigations reported in the paper, with the considered parameters highlighted ("•" investigated parameters; "-" neglected parameters)

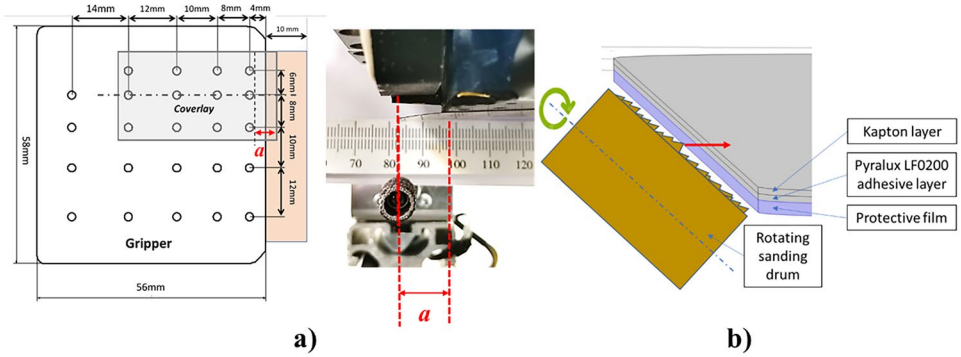


**Fig. 6** Details of coverlay gripping and pre-peeling mechanics. **a** Vacuum orifice pattern and coverlay positioning. **b** Detail view of the mechanical peeling action and scheme of the sanding drum-coverlay interaction

drum, whose rotation is provided by a DC motor with an encoder controlled in a closed loop.

## 2.1 Numerical simulations

A parametric linear FEM model of the coverlay-system is developed in the COMSOL Multiphysics v.5.5 environment to evaluate the coverlay stiffness in response to the triggering force in different gripping conditions. The relevance of stiffness is due to the fact that, since a stiffer material can bear higher loads before bending, the arise of breaking mechanisms is favored. As per the pre-peeling process, in the model, the coverlay is gripped on the side of the Kapton layer with a predefined overhanging portion, identified by the parameter $a$ (see Fig. 6). The FEM model of the film component presents the three layers, with material mechanical properties summarized in Table 1.

In consideration of the flatness of the layers, more than 300,000 tetrahedral elements is used to discretize the geometry. The solution of each configuration of the FEM model, consisting of more than 1.4 million degrees of freedom, required less than 4 min of processing time on a 6-cores Intel i7@2.20 GHz CPU platform.

To replicate the gripping conditions, the suction cups are modeled as fixed constraints where the middle row is placed at the coverlay mid-plane; to simulate the action of the sanding drum, a point load of 1 N is applied at the bottom edge of the coverlay. Therefore, the total displacement of the point load is evaluated (see Fig. 7), and the stiffness is then calculated as the ratio between the load and the total displacement. The FEM model considers two different adhesive thicknesses, three gripping positions, and five load positions along the bottom edge of the protective film. Since the sanding particle can randomly hit the protective film at any point along the bottom edge, this latter parameter in particular enables to assess the potential influence of process randomness on the overall stiffness and, thus, on process repeatability. Parameter values are reported in Table 2.

The graphs of the simulation results are reported in Fig. 8 and the values are reported in the Table 6 in Appendix. The stiffness strongly decreases with the increase of the overhanging length and when the adhesive thickness is reduced. In particular, when the overhanging length is increased from $a = 5$ mm to $a = 10$ mm, the overall stiffness reduces of about one half. The obtained stiffness values suggest that for an overhanging length $a = 5$ mm, the pre-peeling process is much more favored than in the other cases.

**Table 1** Mechanical properties of materials

| Material | Young's modulus E [MPa] | Poisson's ratio ν |
|---|---|---|
| DuPont Kapton | 4500 | 0.34 |
| Pyralux LF0200 adhesive layer | 2800 | 0.34 |
| Polyethylene protective film layer | 219 | 0.34 |

Source: Dupont datasheets. Polyethylene data gathered from www.matweb.com

## 2.2 Experimental procedure

A typical pre-peeling task consists in the following sequence:

1. coverlay pick by the robot;
2. positioning on top of the pre-peeling station with proper configuration;
3. downward motion towards the sanding drum until a predefined position along the $z$-axis;
4. pre-peeling: an overhanging portion of the coverlay collides with the rotating sanding drum;
5. upward motion;
6. release of the coverlay; and

**Table 2** FEM model parameters

| Parameters | Symbol | Values [mm] |
|---|---|---|
| Coverlay thickness | $t_C$ | 0.125, 0.100 |
| Overhanging length | $a$ | 5, 10, 15 |
| Distance of load application | $d\_Load$ | −12, −7, 0, 7, 12 |

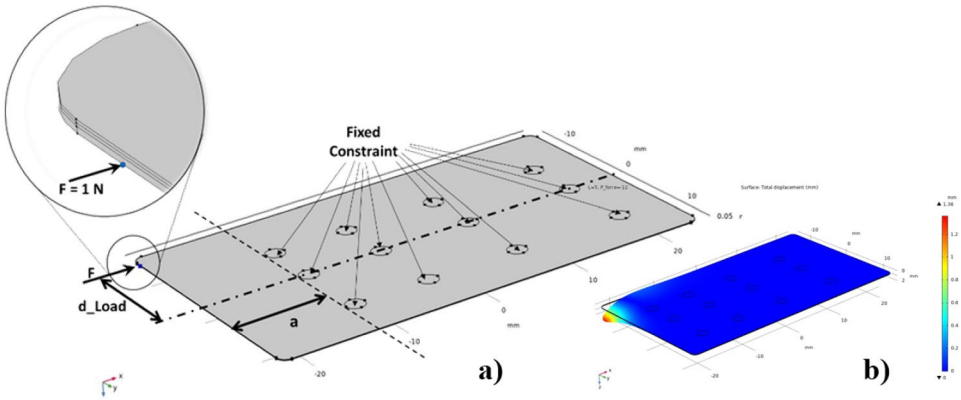


**Fig. 7** FEM boundary conditions. **a** Force applied at a "*d_Load*" distance from the reference plane of the vacuum orifices pattern, which represents the fixed constraints (null displacement). **b** Typical shaded plot of total displacement parameter

7. assessment of the Peeled Area Rate (*PR*), defined as the ratio between the protective film area actually detached (Peeled Area, *PA*) and the total coverlay area (Total area, *TA*).

With reference to points 2 and 3, the actual mutual position of the coverlay and the sanding drum can be different from the set one, due to the deflection of the overhanging portion of the picked coverlay. To deal with this issue, the configuration of the robot was adjusted depending on the overhanging coverlay length by applying a compensation, as hereafter described. The programmed impact point is set at the top of the sanding drum, with the coverlay tip that moves in the vertical *zx*-plane passing through the tool axis. In Fig. 9, such a test sequence is depicted, with the relevant parameters highlighted:

(a) thickness of the coverlay adhesive ($t_A$);
(b) unsupported overhanging portion of the coverlay out of the vacuum gripper ($a$);
(c) angular speed of the rotating sanding drum ($\omega_s$);
(d) radius of the sanding drum ($r$);
(e) roughness of the sanding drum ($gr$);
(f) robot *Z*-axis approaching speed ($v_R$);
(g) compensation along *X*-axis $x_C(a)$; and
(h) compensation $z_C(a)$ of the quote of the gripper during pre-peeling.

To investigate the influence of the process parameters on the "pre-peeling" phase, an experimental campaign was designed and performed. To verify the optimal value of parameter $a$ obtained by the numerical simulations, preliminary tests were performed on rectangular coverlays (Dupont™ Pyralux LF 0110 and LF 0210 with size of 25 × 40 mm). The values of 5 and 10 mm were investigated and the measured success rates (corresponding to successful detachments with $PR > 5\%$) were 98% and 78%, respectively. The threshold value of 5% was chosen considering that it corresponds to the minimum area required to enable the completion of the next peeling task performed by a small 5-mm-diameter vacuum cup. In fact, the value of 5% guarantees a pre-peeled area of 50 mm$^2$ (5% of 25 × 40 mm), which, in the worst case, results in a rectangular pre-peeled area of 25 × 2mm. Using a vacuum cup having a radius of 2.5 mm, acting on the pre-peeled portion of 2 mm succeeds in the final removal of the protective film. However, this threshold should be tuned for each specific coverlay shape and size. The value that guarantees a higher success percentage in removing the protective film was $a = 5$ mm, confirming the numerical results presented in Sect. 2.1.

Therefore, a suitable experimental design was adopted (Sect. 2.3) to characterize the device and investigate the effects of the working parameters on the pre-peeling process performance (*PA* and *PR*), in order to define the best parameter combination for the protective film removal.

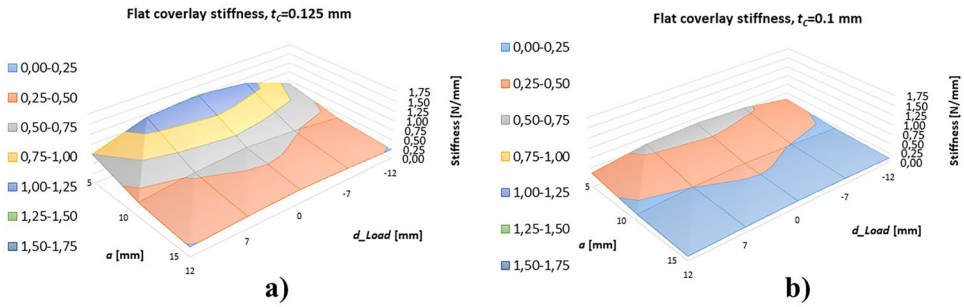


**Fig. 8** Graphs of the flat coverlay stiffness at different values of parameter $a$. **a** Coverlay thickness $t_C = 0.125$ mm, **b** Coverlay thickness $t_C = 0.100$ mm. Numerical values reported in Table 6 in Appendix

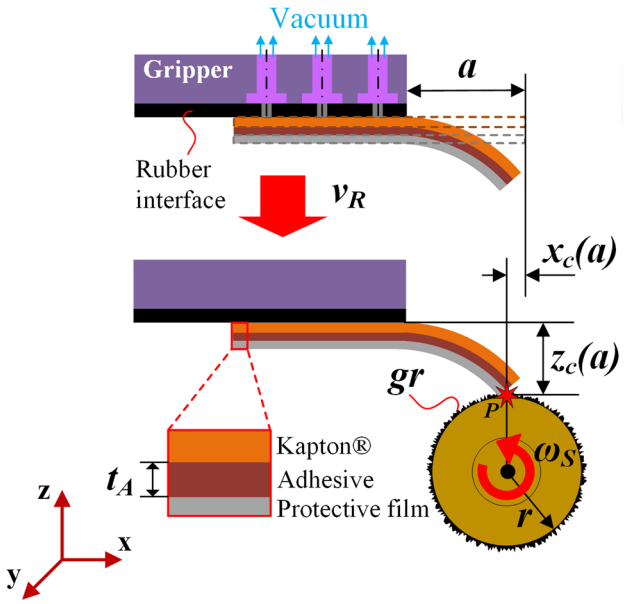


**Fig. 9** Pre-peeling strategy and working parameters

The geometry of all the tested samples was rectangular, 27.2 × 46.4 mm, and then the gripper picking configuration (i.e., the pattern type and the number of the vacuum orifices activated) was set constant for all the tests. In accordance with typical product specifications of FPCBs (courtesy of Somacis S.p.A., Italy), two different

**Table 3** Experimental design summary

| Factor | Symbol | Levels | | |
|---|---|---|---|---|
| Adhesive thickness (μm) | $t_A$ | 25 | 50 | – |
| Sanding drum rotational speed (rpm) | $\omega_S$ | 550 | 700 | 850 |
| Robot speed (mm/s) | $v_R$ | 18 | 180 | – |

Kapton-based coverlay materials were tested, Dupont Pyralux LF 0110 and LF 0210, presenting different thickness *t* of the adhesive substrate (25 μm and 50 μm, respectively). Considering the three layers (Kapton, acrylic adhesive, protective film), the former has a total thickness of 100 μm (25 + 25 + 50), while the latter is 125 μm thick (25 + 50 + 50). The experimental campaign was performed at standard environmental conditions (i.e., 20–23 °C and 0–10% RH).

As output of the tests, the *PR* of the film removal was assessed. To measure the *PA*, a picture of the coverlay was acquired with a vision system having the following features: (i) resolution 1440 × 1080 and (ii) field of view 65.5 × 49.2 mm; spatial resolution of 0.045 mm/pixel [21]. The vision system was calibrated, adopting the methodology proposed by [22], with an error of 0.05 mm. The image is post-processed with edge detection and gauging Matlab algorithms (see Fig. 10). The acquired images were manipulated before the post-processing to highlight the profiles of the detached portions of the coverlays.

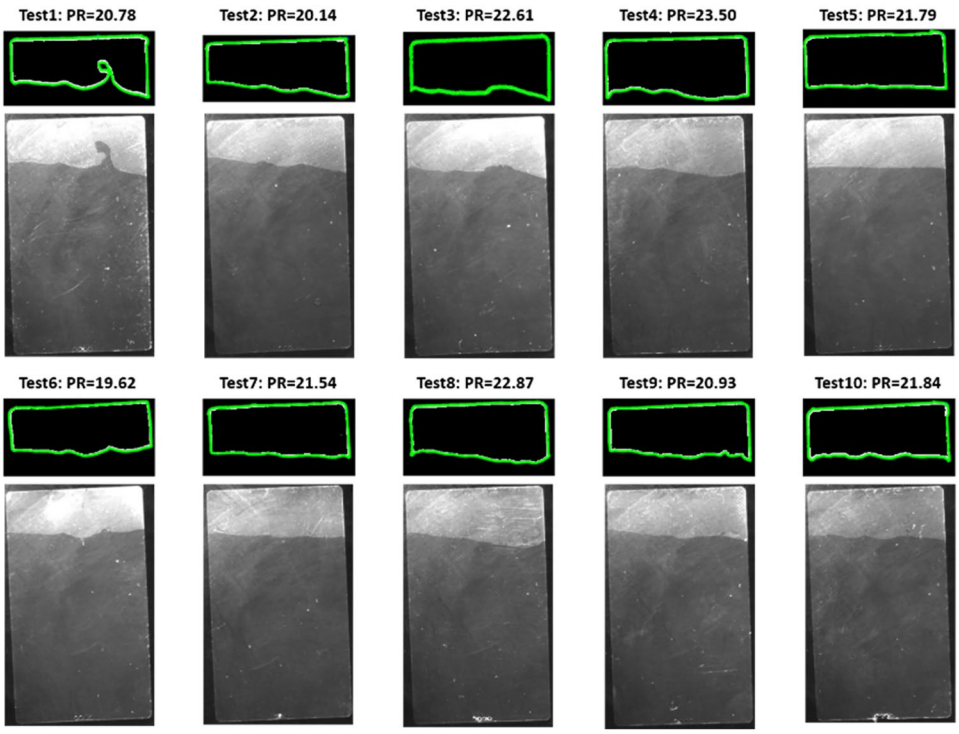


**Fig. 10** Image processing for the calculation of the *PA*

**Table 4** Constant parameters

| Parameter | Symbol | Value |
|---|---|---|
| Coverlay overhanging length (mm) | $a$ | 5 |
| Sanding drum radius (mm) | $r$ | 8 |
| Sanding drum roughness (grit size) | $gr$ | 60 |

### 2.3 Experimental design

The effects of the selected parameters on the performance of the fully automated pre-peeling process were studied using a suitable experimental design (Table 3). The three selected factors are the adhesive thickness ($t_A$), the rotational speed of the sanding drum ($\omega_S$), and the robot speed ($v_R$). Table 4 summarizes the constant parameters of the experimental design (see Sect. 2.2).

The two selected levels of $t_A$ correspond to the two tested materials (Sect. 2.2). Three levels were selected for $\omega_S$, based on the previous experimental campaigns [12, 13]. Two different robot approaching velocities $v_R$ were tested, considerably varying one from each other: the lowest one (18 mm/s) representing a "safe" velocity for pre-peeling success and the highest one (180 mm/s) considering the implementation of the pre-peeling in an automated process. Five replicates were carried out for each of the 12 experimental conditions; hence, the whole experimental design included 60 runs. The replicates were assumed as blocks, and the runs were randomized within each block. The analysis of variance (ANOVA) analyzed the response on the performance parameter *PR*.

## 3 Results and discussion

A suitable model was analyzed to study the effect of the factors listed in Table 3 on *PR*. Table 5 summarizes the ANOVA results, showing the statistically significant factors, while the plots in Fig. 11 depict the results related to *PR* for each factor.

**Table 5** ANOVA $p$ values for the analysis on the peeled area rate. (bold = significant factor, confidence level $\alpha = 0.1$)

| Factors | Symbol | *P* value |
|---|---|---|
| Blocks | | 0.249 |
| Main factors | $t_A$ | **0.089** |
| | $\omega_S$ | 0.417 |
| | $v_R$ | 0.468 |
| Interactions | $t^*\omega_S$ | 0.259 |
| | $t^*v_R$ | 0.895 |
| | $\omega_S{}^*v_R$ | 0.870 |

Based on the ANOVA results (Table 5), the response is affected only by the adhesive resin thickness $t_A$. Figure 11a shows that as $t_A$ increases, the peeled area rate decreases. This behavior can be explained by the fact that the trigger load increases with increasing adhesive thickness, especially in the range of 0.01–0.08 mm, as reported by Roskowicz et al. in [23]. The results also reveal that the robot approaching velocity $v_R$ does not influence the *PA*; thus, it can be reasonably set at high values in order to reduce the task execution time. Likewise, the rotational speed of the sanding drum is not significant in terms of peeled area response. This latter result suggests that the mechanism of the detachment process is mainly affected by the coverlay material properties (above all, its stiffness) rather than the trigger force magnitude exerted by the sanding drum. In view of the flexibility of the coverlay, a random sanding particle enforces a displacement of a random point on the bottom edge of the protective film, thus deforming the coverlay. At the same time, the deformation generates internal stress on the adhesive layer, which results in the separation of the protective film. The stress induced by the deformation is mainly determined by the coverlay overall stiffness: the higher is the stiffness, the higher is the induced stress and the success probability of the pre-peeling process. However, it is also worth observing that different thicknesses of the adhesive layer correspond to different behaviors in the pre-peeling process. In fact, a thicker ply of adhesive requires a higher trigger load, and it distributes the stress more effectively than a thinner layer, reducing the local stress concentration, which causes the detachment. Therefore, it is expected that, by changing the adhesive layer thickness, a different coverlay stiffness level is required to trigger the detachment.

The experimentation reveals a certain scattering of the *PA* values for the same set of parameters. To discuss this result, it is worth considering the numerical simulations reported in Sect. 2.1 and, in particular, the stiffness variation along the coverlay edge. Considering, indeed, that the impact of the sanding grain can occur at any point of the entire coverlay edge, as *d_load* varies within the range of $-12/+12$ mm, the overall stiffness can be dramatically different depending on *d_load*, consequently affecting the *PA*. From the simulations, it is also possible to notice that, regardless the value of the parameter $a$, promoting the impact in a position close to the symmetry axis (*d_load* = 0 mm) would result in higher success rates and a general improvement of *PA*. As a conclusion of this analysis, the position of the sanding drum and the reduction of its axial length are fundamental for an optimal process setup.

A further factor influencing process variation is the coverlay curvature: considering that coverlay sheets are usually obtained by coils, suitable for roll-to-roll processes, a pre-strain (residual curvature) may affect the

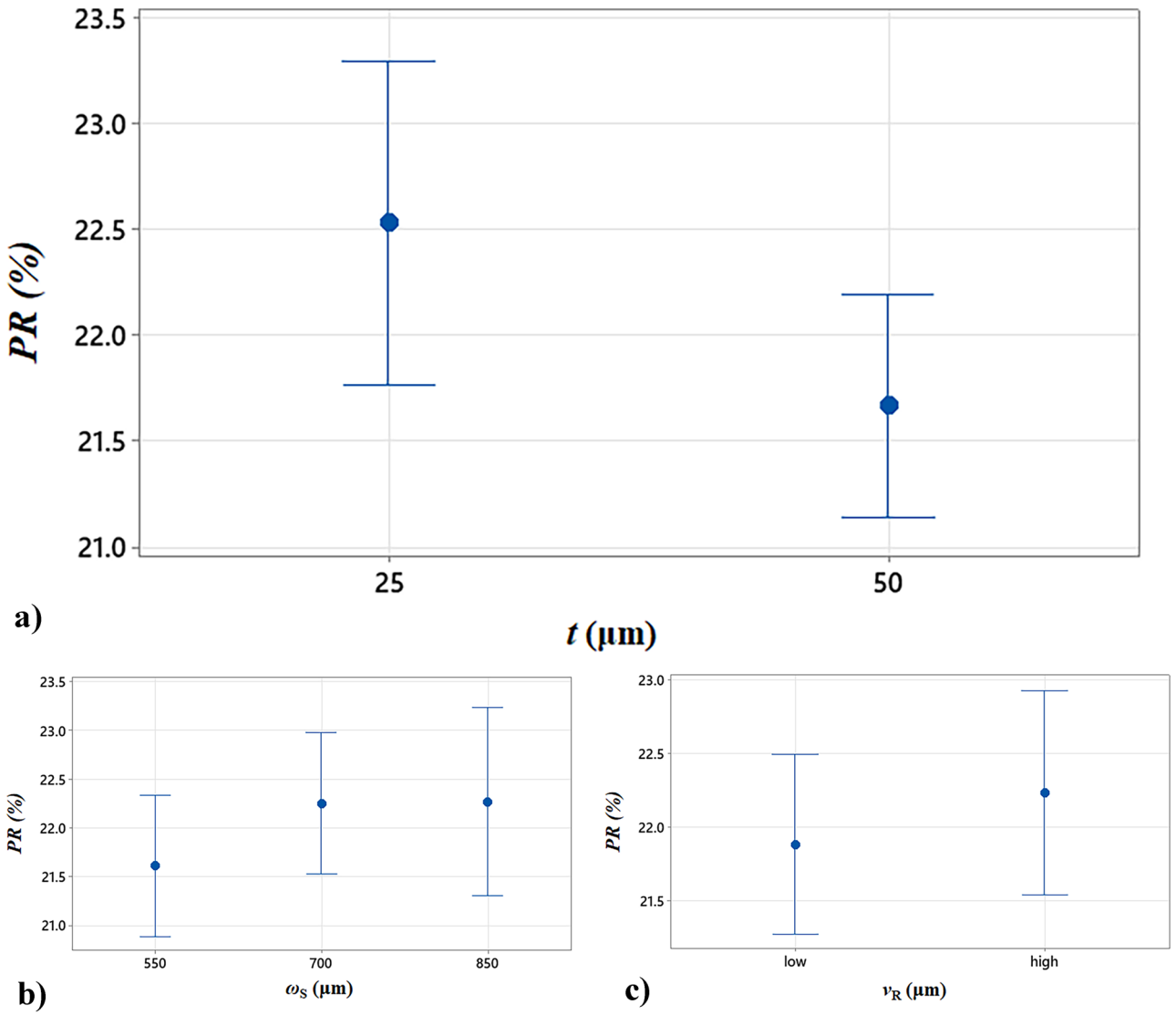


**Fig. 11** Interval plot of the peeled area rate against the adhesive resin thickness (**a**), rotational speed of the sanding drum (**b**), and robot approaching speed (**c**)

coverlays geometry. Such a curvature may have different directions, depending on the coverlay position, and orientation in the sheet. To analyze this effect, further parametric calculations were performed, considering a curvature radius of 100 mm and two orientations: along *X* and *Y* axes. In the numerical model, it is assumed that the suction cups constraint the coverlay to be flat only partially, as shown in Fig. 12.

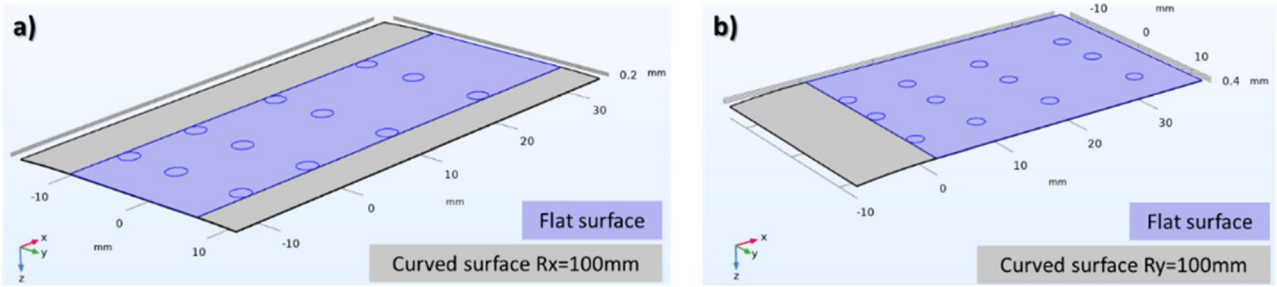


**Fig. 12** Curved coverlays and constrained flat surfaces. **a** Curvature around the *x* axis with radius $R_x = 100$ mm. **b** Curvature around the *y*-axis with radius $R_y = 100$ mm

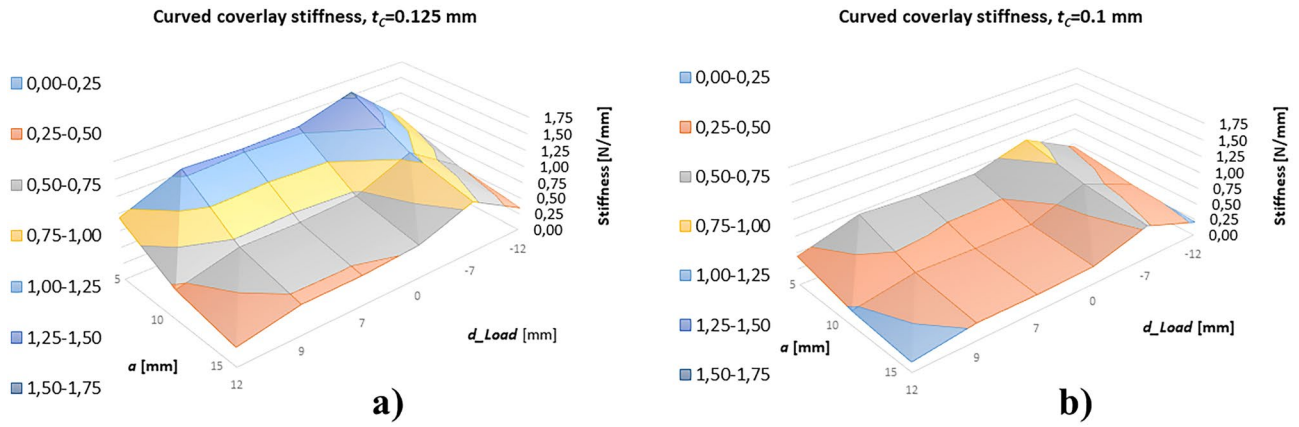


**Fig. 13** Graphs of the curved coverlay stiffness ($R_x$ = 100 mm) at different values of "*a*": **a** coverlay thickness $t_C$ = 0.125 mm, **b** coverlay thickness $t_C$ = 0.100 mm

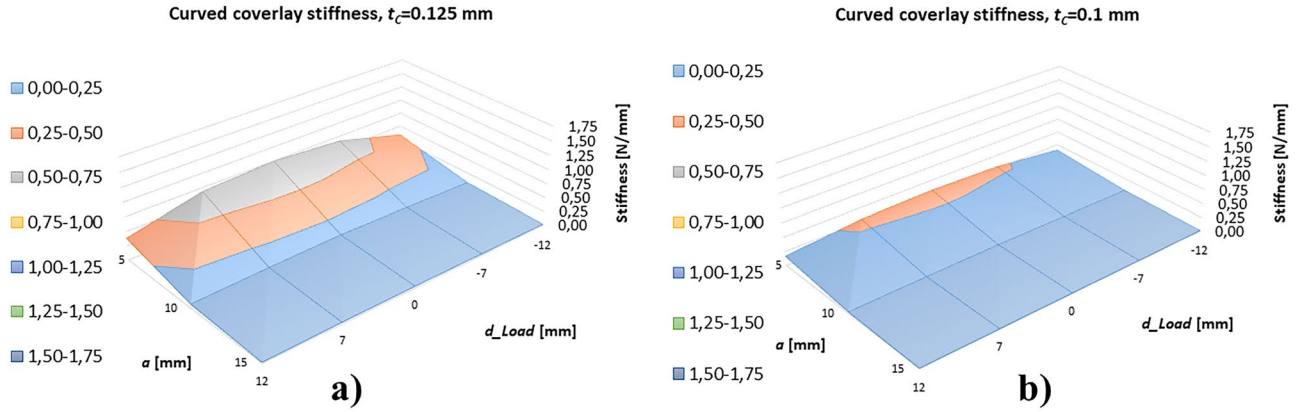


**Fig. 14** Graphs of the curved coverlay stiffness ($R_y$ = 100 mm) at different values of "*a*". **a** Coverlay thickness $t_C$ = 0.125 mm. **b** Coverlay thickness $t_C$ = 0.100 mm

In particular, in the case of *X* curvature orientation, the curved surfaces are 7 mm wide for negative values of *y*, and 5 mm wide for positive values of *y*.

Figures 13 and 14 (numerical values in Table 7 in Appendix) report the stiffness calculated for all parameters, both curvatures (along *X* and *Y* axes) and considering a load of 1 N oriented in X direction.

The stiffness map reveals that the coverlay residual curvature and its orientation are very important. In fact, a curvature along the *Y*-axis with a radius of only 100 mm can dramatically reduce the stiffness. On the contrary, a curvature oriented along the *X*-axis can slightly increase the coverlay stiffness. Therefore, the coverlay curvature and its orientation should be taken into account, in order to improve the *PA* and process control. In view of this result, it is important to opportunely measure and control the curvature orientation and amplitude. This also suggests new insights for gripper design: a properly curved interface would indeed constrain the coverlay to a higher stiffness configuration and more reliable pre-peeling.

A latest investigation aims at evaluating if, in the case of *Y*-curved coverlays, an opportune compensation rotation of the coverlay approaching the sanding drum (corresponding to a different robot approaching configuration) can lead to some benefits to the process. This is simulated with a load tangent to the coverlay on its edge. This condition seems to be notably effective due to the increase of the coverlay stiffness in the case of $a$ = 5 mm (results in Table 8 in Appendix).

This result shows that a coverlay curvature compensation, performed by a 6-DOF handling system, can be a successful strategy for improving the pre-peeling process.

## 4 Conclusion

This paper investigates the effects of different parameters in the pre-peeling phase of the automated assembly of film-based coverlays, as proposed in previous works [12, 13], to be implemented in FE production. Since the

pre-peeling process is evidently stochastic, the investigation is focused on different parameters affecting process success and effectiveness.

Once defined an optimal process configuration (overhanging length of the coverlay *a*) by preliminary FEM analysis, a test campaign was performed, considering material-related parameters (adhesive thickness), and process-specific parameters (approach velocity of the robot and rotating velocity of the sanding drum). As output of the experimental campaign, the percentage of *PA* was assessed at each run, and analyzed through the ANOVA method. The analysis led, first of all, to notice the relevance of the system stiffness on the process, while the two velocities did not considerably impact the process output. In relation to this, higher values of adhesive thickness $t_A$ correspond to lower *PA*; this can be a relevant process-related indication to be considered during the design of the FE products. On the other hand, the negligible effect of the robot velocity allows to consider that the pre-peeling process, implemented in the whole automated assembly, would not represent a process bottleneck, thus enabling high throughputs.

The experimental campaign reveals the low impact of the velocities, highlighting that only component-related parameters mainly affect the process and, in particular, the stiffness exhibited by the component in response to the pre-peeling triggering force. Such a stiffness depends on the configuration of the process (*a*) and material-specific parameters ($t_A$), including in this case also the pre-strain component due to its procurement conditions (thus considering pre-strain radii $R_x$ and $R_y$). The following conclusions are drawn in relation to component stiffness:

- the local stiffness at the application point of the trigger force can vary significantly, thus affecting the process: points on coverlay edge in proximity to the central axis are characterized by higher stiffness, thus suggesting modifying the process setup to promote the pre-peeling in this area;
- the pre-strain (curvature) due to material procurement and stocking cannot be neglected due to its direct influence on the mutual orientation of the triggering force and the coverlay edge.

These considerations lead to the following relevant outlook measures to be implemented in the process:

- the sanding tool should be adjusted and reduced in length to enable its optimal positioning (central axis) with regard to the coverlay edge;
- the curvature along the *y*-axis should be compensated during the manipulation by properly configuring the gripper before approaching the sanding drum;
- the curvature along the *x*-axis increases the longitudinal stiffness, suggesting that a specific design of coverlay gripper interface, with the same (or similar) curvature, would improve the process effectiveness.

Leveraging all these new results and knowledge on the process, a further future work will be focused on how to incorporate the effect of curvature, compensating the pre-strain on the coverlay by exploiting the degree of freedom of the robotic arm and optimizing the sanding drum dimensions and the gripper design.

## Appendix

**Table 6** Stiffness of flat coverlay

| **Flat coverlay stiffness [*N*/mm]** | | | | | | | | | | |
|---|---|---|---|---|---|---|---|---|---|---|
| **$t_C$ = 0.125 mm** | | ***d_Load* [mm]** | | | | | **Mean value** | **Std dev** | **Min** | **Max** |
| | | *−12* | *−7* | *0* | *7* | *12* | | | | |
| ***a* [mm]** | *5* | 0.66 | 1.12 | 1.27 | 1.17 | 0.75 | 0.99 | 0.27 | 0.66 | 1.27 |
| | *10* | 0.37 | 0.52 | 0.61 | 0.53 | 0.38 | 0.48 | 0.10 | 0.37 | 0.61 |
| | *15* | 0.24 | 0.30 | 0.35 | 0.31 | 0.24 | 0.29 | 0.05 | 0.24 | 0.35 |
| **$t_C$ = 0.1 mm** | | ***d_Load* [mm]** | | | | | **Mean value** | **Std dev** | **Min** | **Max** |
| | | *−12* | *−7* | *0* | *7* | *12* | | | | |
| ***a* [mm]** | *5* | 0.32 | 0.54 | 0.61 | 0.56 | 0.36 | 0.48 | 0.13 | 0.32 | 0.61 |
| | *10* | 0.17 | 0.25 | 0.29 | 0.25 | 0.18 | 0.23 | 0.05 | 0.17 | 0.29 |
| | *15* | 0.11 | 0.14 | 0.16 | 0.14 | 0.11 | 0.13 | 0.02 | 0.11 | 0.16 |

**Table 7** Stiffness of curved coverlay along $x$ and $y$ axes ($R_x = R_y = 100$ mm)

| **Curved $R_x = 100$ mm coverlay stiffness [N/mm]** | | | | | | | | | | |
|---|---|---|---|---|---|---|---|---|---|---|
| **$t_C = 0.125$ mm** | | ***d_Load* [mm]** | | | | | **Mean value** | **Std dev** | **Min** | **Max** |
| | | *−12* | *−7* | *0* | *7* | *12* | | | | |
| ***a* [mm]** | *5* | 0.86 | 1.55 | 1.30 | 1.28 | 0.94 | 1.20 | 0.26 | 0.86 | 1.55 |
| | *10* | 0.52 | 1.05 | 0.72 | 0.68 | 0.46 | 0.69 | 0.21 | 0.46 | 1.05 |
| | *15* | 0.34 | 0.80 | 0.52 | 0.46 | 0.29 | 0.48 | 0.18 | 0.29 | 0.80 |
| **$t_C = 0.1$ mm** | | ***d_Load* [mm]** | | | | | **Mean value** | **Std dev** | **Min** | **Max** |
| | | *−12* | *−7* | *0* | *7* | *12* | | | | |
| ***a* [mm]** | *5* | 0.45 | 0.88 | 0.64 | 0.65 | 0.44 | 0.63 | 0.16 | 0.44 | 0.88 |
| | *10* | 0.30 | 0.65 | 0.36 | 0.36 | 0.23 | 0.38 | 0.14 | 0.23 | 0.65 |
| | *15* | 0.21 | 0.52 | 0.28 | 0.26 | 0.15 | 0.28 | 0.13 | 0.15 | 0.52 |
| **Curved $R_y = 100$ mm coverlay stiffness [*N*/mm]** | | | | | | | | | | |
| **$t_C = 0.125$ mm** | | ***d_Load* [mm]** | | | | | **Mean value** | **Std dev** | **Min** | **Max** |
| | | *−12* | *−7* | *0* | *7* | *12* | | | | |
| ***a* [mm]** | *5* | 0.33 | 0.66 | 0.75 | 0.68 | 0.39 | 0.56 | 0.19 | 0.33 | 0.75 |
| | *10* | 0.07 | 0.11 | 0.13 | 0.11 | 0.07 | 0.10 | 0.03 | 0.07 | 0.13 |
| | *15* | 0.02 | 0.03 | 0.04 | 0.03 | 0.02 | 0.03 | 0.01 | 0.02 | 0.04 |
| **$t_C = 0.1$ mm** | | ***d_Load* [mm]** | | | | | **Mean value** | **Std dev** | **Min** | **Max** |
| | | *−12* | *−7* | *0* | *7* | *12* | | | | |
| ***a* [mm]** | *5* | 0.14 | 0.28 | 0.32 | 0.29 | 0.17 | 0.24 | 0.08 | 0.14 | 0.32 |
| | *10* | 0.03 | 0.04 | 0.06 | 0.05 | 0.03 | 0.04 | 0.01 | 0.03 | 0.06 |
| | *15* | 0.01 | 0.01 | 0.01 | 0.01 | 0.01 | 0.01 | 0.00 | 0.01 | 0.01 |

**Table 8** Stiffness of coverlay with compensation of curvature along $y$-axis ($R_y = 100$ mm)

| **Curved $R_y = 100$ mm coverlay stiffness [*N*/mm], and tangent load** | | | | | | | | | | |
|---|---|---|---|---|---|---|---|---|---|---|
| **$t_C = 0.125$ mm** | | ***d_Load* [mm]** | | | | | **Mean value** | **Std dev** | **Min** | **Max** |
| | | *−12* | *−7* | *0* | *7* | *12* | | | | |
| ***a* [mm]** | *5* | 1.04 | 4.91 | 4.30 | 4.40 | 4.81 | 3.89 | 1.61 | 1.04 | 4.91 |
| | *10* | 0.18 | 0.32 | 0.51 | 0.36 | 0.20 | 0.32 | 0.13 | 0.18 | 0.51 |
| | *15* | 0.04 | 0.06 | 0.08 | 0.07 | 0.05 | 0.06 | 0.02 | 0.04 | 0.08 |
| **$t_C = 0.1$ mm** | | ***d_Load* [mm]** | | | | | **Mean value** | **Std dev** | **Min** | **Max** |
| | | *−12* | *−7* | *0* | *7* | *12* | | | | |
| *a* **[mm]** | *5* | 0.45 | 3.10 | 2.45 | 2.47 | 1.72 | 2.04 | 1.01 | 0.45 | 3.10 |
| | *10* | 0.08 | 0.13 | 0.20 | 0.14 | 0.08 | 0.12 | 0.05 | 0.08 | 0.20 |
| | *15* | 0.02 | 0.02 | 0.03 | 0.03 | 0.02 | 0.02 | 0.01 | 0.02 | 0.03 |

**Acknowledgements** The authors acknowledge Mr. Paolo Scalmati (SOMACIS S.p.A., Italy) for the precious support in FPCB specifications and components selection and Eng. Francesco Giacomini (Camozzi Automation S.p.A., Italy) for the support provided on pneumatic solenoid valves selection and supply.

**Author contribution** The study conception and design were performed by Vito Basile, Francesco Modica, Gianmauro Fontana, and Marcello Valori. Material preparation and experimental campaign were performed by Gianmauro Fontana, Simone Pio Negri, Marcello Valori, Vito Basile, and Serena Ruggeri. Data collection and analysis were performed by Lara Rebaioli, Vito Basile, Marcello Valori, Gianmauro Fontana, and Francesco Modica. Numerical analysis was performed by Francesco Modica. The first draft of the manuscript was written by Vito Basile, Francesco Modica, Marcello Valori, and Gianmauro Fontana. Scientific coordination was performed by Irene Fassi and Vito Basile. All authors commented on previous versions of the manuscript. All authors read and approved the final manuscript.

**Funding** This research was partially funded by the Italian Government through the Program H2020 PON 2014–2020, within the project "High-performance electronic Embedded Systems (HELMS)" under grant no. F/050507/02–03/X32.

## Declarations

**Competing interests** The authors declare no competing interests.

## References

1. Cai S, Han Z, Wang F, Zheng K, Cao Y, Ma Y, Feng X (2018) Review on flexible photonics/electronics integrated devices and fabrication strategy. Sci China Inf Sci 61:1–27
2. European Commission (2019) Report on the Flexible and Printed Electronics Workshop. [Online]. Available: https://ec.europa.eu/digital-single-market/en/news/report-flexible-and-printed-electronics-workshop. [Accessed Jan 2021]
3. Ruggeri S, Fontana G, Basile V, Valori M, Fassi I (2017) Micro-robotic handling solutions for PCB (re-)Manufacturing. Procedia Manuf 11:441–448
4. Fontana G, Ruggeri S, Fassi I (2014) Precision handling of electronic components for PCB rework. IFIP Adv Inf Commun Technol 435:52–60
5. Salleo A, Wong WS (2009) Flexible electronics: materials and applications. Springer
6. Coombs CF, Holden H (2016) Printed circuits handbook, 7th ed. McGraw-Hill Education
7. Gengenbach U et al (2020) Automated fabrication of hybrid printed electronic circuits. Mechatronics 70:102403
8. Gengenbach U et al (2019) Automated fabrication of multi-layer printed electronic circuits using a novel vector ink-jet printing process control and surface mounting of discrete components. IFAC-PapersOnLine 52(15):609–614
9. Bian J et al (2019) Laser transfer, printing, and assembly techniques for flexible electronics. Adv Electron Mater 5(7):1800900
10. Shin D et al (2010) A FPCB cutting process using a pico-second laser. J Laser Micro/Nanoeng 5:48–52
11. Cui Z (2016) Printed electronics: materials, technologies and applications. John Wiley & Sons
12. Valori M, Basile V, Negri SP, Scalmati P, Renghini C, Fassi I (2021) Towards the automated coverlay assembly in FPCB manufacturing: concept and preliminary tests. In: Ratchev S. (eds) Smart Technologies for Precision Assembly. IPAS 2020. IFIP Adv Inf Commun Technol 620:36–50. Springer, Cham. https://doi.org/10.1007/978-3-030-72632-4_3
13. Valori M, Basile V, Ruggeri S, Fontana G, Negri SP, Alberola JAM, Fassi I (2021) Assembly of film coverlays: development of a configurable gripper for process automation. Procedia Manuf 55:80–87
14. Toyoda Y, Tanaka N (2009) Method and apparatus for producing a wiring board, including film-peeling. U.S. Patent No. 7,481,901
15. Ahn KH (2014) Method and apparatus for peeling donor film from substrate. U.S. Patent No. 8,877,006
16. Björnsson A, Lindbäck JE, Johansen K (2013) Automated removal of prepreg backing paper-a sticky problem. SAE 2013 Aerotech Congress and Exhibition, 24–26 Sep 2013, Montréal, Quebec, Canada
17. Kupzik D, Ballier F, Lang J, Coutandin S, Fleischer J (2018) Development and evaluation of concepts for the removal of backing foils from prepreg for the automated production of UD reinforced SMC parts. ECCM 2018 - 18th European Conference on Composite Materials, 24-28 Jun 2018, Athens, Greece
18. Björnsson A, Jonsson M, Eklund D et al (2017) Getting to grips with automated prepreg handling. Prod Eng Res Devel 11:445–453. https://doi.org/10.1007/s11740-017-0763-2
19. Li S et al (2017) Shear deformation dominates in the soft adhesive layers of the laminated structure of flexible electronics. Int J Solids Struct 110:305–314
20. Jo W, Lee T-I, Kim T-S (2022) Enlarged tensile strain at edge of flexible substrate due to anticlastic curvature. Microelectron Reliab 130:114485
21. Modica F et al (2018) Can a low cost sensing system be exploited for high precision machining? Procedia CIRP 75:391–396
22. Fontana G, Ruggeri S, Legnani G, Fassi I (2018) Unconventional calibration strategies for micromanipulation work-cells. Robotica 36(12):1897–1919
23. Roskowicz M, Godzimirski J, Komorek A, Jasztal M (2021) The effect of adhesive layer thickness on joint static strength. Materials 14(6):1499